NASA CR-

GA-6832

TOPICAL REPORT

THE ENERGY DEPENDENCE OF THE NEUTRON CAPTURE CROSS SECTION OF THE TUNGSTEN ISOTOPES FROM .01 TO 10 EV

by

S. J. Friesenhahn
E. Haddad
F. H. Fröhner
W. M. Lopez

prepared for

NATIONAL AERONAUTICS AND SPACE ADMINISTRATION

Contract SNPC-27

Technical Management
NASA-Lewis Research Center
Cleveland, Ohio
Nuclear Reactor Division
D. Bogart

GENERAL ATOMIC
DIVISION OF
GENERAL DYNAMICS

JOHN JAY HOPKINS LABORATORY FOR PURE AND APPLIED SCIENCE

P.O. BOX 608, SAN DIEGO, CALIFORNIA 92112

ABSTRACT

14916

Capture cross section measurements from 0.01 to 10. eV on W^{182}, W^{183}, W^{184} and W^{186} employing a totally absorbing gamma ray detector are described. The 2200 m/sec value of the capture cross section is compared with previously reported measurements, and the shape and magnitude of the cross section curve is compared to calculations using reported resonance parameters. Parameters of negative energy levels required to account for the discrepancy between measured and calculated cross sections for W^{182} and W^{184} are given. A measurement of the gold capture cross section is used as a check on the techniques employed.

Author

I. INTRODUCTION

Tungsten has become of interest as a structural material for high temperature reactors due to its very high melting point. Since the thermal neutron capture cross section of tungsten is not small it is important to have accurate capture cross sections in the region of the Maxwellian neutron velocity distribution. Due to the large temperature difference between startup and operation, the energy dependence of the capture cross section must be known over an appreciable energy interval. The capture cross section shape may deviate from a 1/v dependence due to both positive and negative energy levels near the neutron binding energy of the compound nucleus, and hence knowledge of the 2200 m/sec value is not sufficient.

Several techniques have been employed to obtain capture cross sections in the low energy region:

1. Pile oscillator technique:[1] This method requires that the cross section have a 1/v dependence, or a known energy dependence with which the value obtained can be corrected.
2. Activation measurements:[2] This technique can be employed to obtain capture cross sections if the decay scheme of the product nucleus is known and if states with suitable half lives are present.
3. Total cross section measurements: Information about the capture cross section can be obtained from this kind of measurement provided the scattering cross section is either small or well known, neither of which is the case for tungsten. Complications arise with this method due to the crystalline binding effects, and hence it is usually the practice to measure

the total cross section at energies below the Bragg cutoff and to extrapolate to thermal energies assuming a 1/v cross section dependence.[3] A correction must still be made for incoherent scattering, however.[4]

4. Calculations using resonance parameters: The low energy cross section can be calculated from measured resonance parameters. However, resonance parameter determinations are subject to analytic and experimental limitations which usually result in undesireably large errors. The calculations are further hampered by the lack of information on resonances outside the measured region, particularly negative energy levels.

Obviously a direct energy-dependent measurement of the capture cross section is desirable. To date there has been no such measurement on any isotope reported in the literature. In this paper we shall describe the capture cross section measurements on the four most abundant tungsten isotopes, W^{182}, W^{183}, W^{184} and W^{186}. No attempt will be made to obtain the cross sections in the Lorentzian part of the low energy resonances, where the multiple scattering effects are large and strongly dependent upon resonance parameters.

II. EXPERIMENTAL TECHNIQUES

A. DETECTOR EFFICIENCY

In the work reported here, the capture cross section was measured by observing the prompt gamma rays which are emitted by the compound nucleus upon neutron capture. In general several gamma rays will be emitted whose spectral distribution is a function of the capturing isotope and the neutron energy. The total energy of the gamma rays is very nearly equal to the neutron binding energy of the compound nucleus. The difference between the prompt gamma ray energy and the neutron binding energy is due to the kinetic energy of the capturing neutron, which is very small at the neutron energies considered here, and may also be due to long lived product nucleus activity. Since it is usually not possible to make corrections for changes in gamma spectra with neutron energy, it is important that the gamma ray detector have a gamma detection efficiency which is independent of the gamma spectrum. This has been achieved by the high efficiency large liquid scintillator which was used in these measurements at General Atomic.[5] A cross sectional view of the scintillator is shown in Fig. 1.

The calculated probability for at least one interaction by a gamma ray before escaping the scintillator is shown in Fig. 2. It is not possible to make a direct experimental check on this calculated intrinsic efficiency since gammas which completely escape obviously cannot contribute to the observed pulse height distribution. It can be noted from the observed pulse height distributions shown in Figs. 3 and 4 that small pulses are relatively infrequent. Since small pulses are due to high energy gammas which lose only a small part of their energy in the scintillator it can be argued that the probability of no pulse at all is also small since energy loss by Compton scattering, which is the dominant process, is a monotonic function of the scattering angle.

A second check can be obtained by observing the capture rate at zero bias for black samples of two different isotopes with markedly different gamma spectra. Since the incident flux is the same, the capture rates will differ by their relative intrinsic efficiencies. A good example is gold, which is known to have a large fraction of high energy gammas and W^{182} which has a much softer spectrum.[6] The observed capture rates agreed to within 2.5%.

It has been experimentally confirmed in every measurement to date that the pulse height distributions due to neutron capture into various resonant states of the same isotope which have the same ingoing orbital angular momenta are identical. An example of this is shown in Fig. 5 for the 4.15 and 21.2 eV levels in W^{182}. This insensitivity to gamma spectra changes due to capture in various resonant states is a strong indication that the fraction of capture events which exceed the lower bias (3 to 4 MeV) will not vary due to the changing contributions to the isotopic cross section from various levels.

B. APPARATUS

The neutron source used in these measurements was the General Atomic linear accelerator. The machine parameters used were: electron energy of 28 MeV, currents of .3 to 1 A, and burst widths of .05 to 4.5 μsec at 22.5 pulses per second. The shorter burst widths were used to reduce the counting rate for the high cross section sample runs and to obtain high resolution flux calibration data. The electron target assembly is shown in Fig. 6. The electrons slowing down in the Fansteel target produce bremsstrahlung which in turn produces high energy neutrons with a broad maximum near 1 MeV. These neutrons were slowed down to the epithermal and thermal region by the water container which also acts as a coolant for the target.

The neutron energy was determined by conventional time-of-flight techniques. The effective flight path length was 18.61 ± 0.01 meters which includes a 0.03 meter correction for neutron slowing down time and the neutron scattering mean free path in the moderator. The entire flight path was maintained at a pressure of less than 150 microns Hg, including an

additional 2.5 meters beyond the sample. The electronics used for the time of flight and pulse height data acquisition are shown in Fig. 7. Not shown are the two independent BF_3 flux monitoring channels which sample the penumbra of the beam just before it enters the scintillator. The sum of the counts in the two monitors was taken to be proportional to the neutron flux at the sample. The signals from the monitors are turned off for 50 μsec following the accelerator burst to eliminate effects due to accelerator noise pickup and bremsstrahlung.

C. FLUX SHAPE

The flux data above 1 eV were taken with two different BF_3 detectors placed at the point at which the neutron beam leaves the scintillator. The smaller of the two was 1 in. in diameter with a 20 cm Hg filling pressure, and the larger one was 2 in. in diameter with a 76 cm Hg filling pressure. The smaller counter was assumed to have a response proportional to the 1/v boron cross section and the larger counter was corrected for self protection which amounted to 3.0% at 1 eV and was proportionately less at higher energies. After this correction the data from both counters could be fitted to a high degree of accuracy by a smoothing function $\Phi(t) = KE^{\alpha}$, where K is a flux normalization constant, E is the neutron energy in eV and α is a constant dependent upon the size and type of moderator.

The determination of the flux shape below 1 eV proved to be more difficult. Consequently five techniques were investigated in an attempt to obtain the relative neutron flux incident on the sample. These techniques consisted in measuring the capture rate in the following absorbers:

1. A 2 in. diameter, .7 in. thick indium disk.
2. Five 2 in. diameter, .1 in. thick indium disks spaced approximately 1 in. apart.
3. A 2 in. diameter, .4 in. thick natural boron disk. (In this measurement the modular construction of the scintillator was utilized by turning off the outer cylinders and using only the central annulus which allowed the low energy boron capture gamma rays to be observed under low background conditions.)

4. A 2 in. diameter, 0.03 in. thick cadmium disk.
5. A 1 in. diameter BF_3 detector with 20 cm Hg filling pressure placed downstream from the sample position.

Methods (1) through (4) depended upon the detection of capture gamma rays in the large liquid scintillator.

The indium disks were "black" (< 1% transmission) below 2 eV, the boron was black below 1.2 eV and the cadmium below .28 eV. All of these black samples were placed at the same location in the scintillator as the capture sample.

There are several possible sources of error in the techniques employing the detection of gamma rays:

1. The gamma biasing efficiency may be neutron energy dependent due to varying contributions to the capture cross section by isotopes with different binding energies.
2. The energy dependence of the fraction of the scattered neutrons which are not captured before leaving the sample.
3. In general some of the capture gammas will be absorbed or degraded in energy before leaving the capturing sample. Since the mean distance that the neutrons penetrate into the sample before the first interaction depends upon the total cross section, the attenuation of the gammas in the sample will be neutron energy dependent. This effect arises from the exponential nature of the attenuation. For s-wave capture the capture gammas are emitted isotropically and hence the gamma transmission for a capture occurring on the surface of an infinite slab can be written:

$$T_s = \frac{1}{2} + \frac{1}{2} \frac{\int_0^1 e^{-\mu d/x} \, dx}{\int_0^1 dx}$$

and at the center:

$$T_c = \frac{\int_0^1 e^{-\mu \frac{d}{2x}} \, dx}{\int_0^1 dx}$$

where

$x = \cos \theta$

μ = effective gamma-ray attenuation coefficient

d = sample thickness

θ = scattering angle

Now $T_c < T_s$ and hence a cross section dependence of the gamma attenuation can be expected.

Effect (1) is small in the case of indium and cadmium since the low energy cross section is dominated by a single low energy resonance. In the case of boron it is completely absent since the branching ratio to the 470 keV level in B^{11} is energy independent in the energy region of interest.

Effect (2) can be estimated from the ratio of scattering to total cross section. This ratio has a maximum value of 1% for cadmium, 3% for indium and 5% for boron. Since a large portion of the scattered neutrons are captured before leaving a black sample, the errors due to this effect should be small compared to the above percentages.

Effect (3) will be small for the .03 in. cadmium since experience has shown that attenuation of gammas in samples of this thickness is small and hence the second order effect described above should be negligible. The .4 in. boron slab is intermediate in thickness. An upper bound on the second order attenuation effect can be obtained by using the mass

absorption coefficient for the 470 keV capture gamma in boron. The difference in transmission for an event at the face of and at the center of an infinite slab is about 5%. Since edge effects and detection of Compton scattered gammas reduce this effect the actual distortion is much less than this even if an extreme change in cross section is assumed, which is of course not the case.

Because of the much higher atomic number of indium and the unknown effective absorption for the capture gamma spectrum, the cross section dependent gamma ray attenuation is not so easy to estimate in this case. Experimental comparisons discussed later will indicate the magnitude of this effect.

The thin BF_3 data were corrected for self protection and absorption in the counter walls using the manufacturer's specifications. The correction was about 1.8% at 0.01 eV.

Figure 8 shows the normalized ratio of the cadmium to boron shapes from 0.01 to 0.28 eV and that of the normalized BF_3 to boron shapes from 0.28 to 1.2 eV. It can be seen that these shapes are consistent within statistics in the regions of comparison, and hence it was concluded that the boron flux shape is correct. Above 0.28 eV the cadmium becomes thin and cannot be used. Below 0.25 eV the BF_3 data showed a systematic departure from the boron and cadmium shapes which was about 3% at 0.01 eV. The reason for this departure is not apparent. The BF_3 was placed in the scintillator in order to check the cross section of the counter walls. Good agreement with the copper cross section was obtained. The absorption in the .02 in. aluminum window at the end of the drift tube could account for only about .1% of the discrepancy. The error could be due to a boron deposit on the inside of the counter wall, but this possibility could not be checked without destroying the tube.

The .7 in. indium flux shape (1) also showed a systematic departure from the boron shape. The deviation shown in Fig. 9 has a shape analogous to the indium cross section which tends to confirm the hypothesis that the

second order gamma attenuation effect discussed is important. The five spaced indium slabs (2) showed a similar deviation which was slightly smaller in magnitude due to the reduced gamma absorption.

One of the best known capture cross sections is that of gold, and hence measurements on gold were included as a check on the techniques employed in the tungsten measurements.

In the case of gold it is possible to obtain information about the capture cross section from the activation cross section since the decay scheme of $_{79}Au^{198}$ is well known.[7] A recent compilation of the low energy cross section data on gold has been made[8] and points derived from a fit to these data are shown in Fig. 10. The calculated capture cross sections obtained from the published resonance parameters using the high and low limits on the product $\Gamma_\gamma \Gamma_n$ for the 4.906 eV resonance, as listed in BNL-325, and the best values of the remaining resonances up to 1 keV, as measured at Saclay[9], are shown in the figure. A statistical calculation[10] was used to include the contribution of resonances above 1 keV. These two curves are reasonably representative of the uncertainty in the calculated cross section since the low energy cross section is dominated by the 4.906 eV resonance. The "total minus scattering" curve was obtained by subtracting the scattering cross section calculated from the above parameters from the total cross section curve of BNL-325. The potential scattering cross section of $11.1 \pm .3$ barns determined by Seth[11] et al., was used in the calculation. The interference between resonant and potential scattering was included only for the 4.906 eV level since the interference contributions of the other levels can be expected to cancel. The data points in the figure were obtained using the boron flux shape described above below 1 eV. The excellent agreement between the data points and the calculated curve tends to confirm the conclusions drawn previously about the reliability of the boron flux shape.

D. FLUX CALIBRATION

The flux shape was made absolute by employing the saturated resonance technique. This involves the measurement of the capture rate

in some energy interval in which the sample transmission is negligible. It is important that capture predominate over scattering to reduce the correction required for neutrons lost from the sample due to scattering collisions, and the thickness of the sample must not be so large as to produce appreciable gamma ray attenuation effects.

These two conditions were fulfilled only by the 4.15 eV resonance in W^{182} and the 4.906 eV resonance in gold for the isotopes investigated in this work. Typical flux calibration data are shown in Fig. 11. The saturated energy interval is indicated by a flattening of the resonance peak. The energy interval indicated in the figure was chosen for the calibration, and the data in this interval were corrected for resolution and multiple scattering[12] effects using the parameters obtained by Bernabie[13] in the case of W^{182}, and the BNL-325[14] parameters for gold. These corrections were from 1 to 3% and are relatively insensitive to the values of the resonance parameters. Hence the error in the calibration correction used is negligible. Since the W^{182} thermal cross section was measured with the same gamma energy bias which was used for the flux calibration, no corrections for biasing efficiency were required for this isotope. The other three tungsten isotopes do not have the same neutron binding energy as W^{182}, and their bias efficiencies cannot be expected to be the same.

In order to correct for these spectral differences, time gated pulse height distributions were taken for captures in the lowest energy resonance in each of the isotopes. In order to minimize errors due to background subtractions the "sliding window" method of background accumulation was employed. In this technique the sample is left in position and the time window is moved to flight times slightly earlier and then slightly later than the time corresponding to the resonance in question. Since the time dependent backgrounds vary only slightly within the width of a typical resonance, the average background accumulated in this fashion is representative of the background in the resonance itself. Using this technique the pulse height data were reliable down to $\approx$1.5 MeV. Below this energy an

extrapolation to zero bias is necessary. As can be seen from the measured pulse height distributions shown in Figs. 3, 4, 5 and 6, a linear extrapolation is consistent with the shape of the distributions. The area under the curves below 1.5 MeV is about 4% of the total. It is highly improbable that the extrapolation could be in error by more than ±50%, and hence a 2% error was assumed.

The exponential flux shape above 1 eV was normalized to the absolute flux at the calibration energy and the boron flux shape was in turn normalized to the exponential flux between 1.05 and 1.20 eV. The measured absolute flux shape is shown as a function of time in Fig. 12.

The gold and natural tungsten data were taken using high purity metallic disks of 2 in. in diameter. The sample thicknesses were 7.294×10^{-4} and 1.795×10^{-3} atoms/barn respectively. The tungsten isotopic cross section data were acquired using tungsten trioxide powder with the thicknesses and enrichments listed in Table 1:

Table 1

Enriched Isotope	ABUNDANCES 180	182	183	184	186	Thickness atoms/barn
182	<.0003	.945	.0209	.0234	.0109	2.423×10^{-3}
183	<.001	.052	.813	.073	.062	8.685×10^{-4}
184	<.0005	.0174	.0174	.942	.0235	2.452×10^{-3}
186	<.001	.0057	.0041	.0183	.972	1.2697×10^{-3}

The trioxide powder was placed in three different types of containments in order to detect errors which might arise due to scattering and capture in the container materials. The containers used were:

1. Pressed cakes with aluminum foil cover
2. Pressed with 10% by weight Plexiglas binder
3. Pressed into thin wall aluminum cans.

The samples in container (1) proved to be extremely fragile and were used only in the first set of measurements. The Plexiglas binder used in containment (2) increased the multiple scattering corrections required by a considerable amount and hence data acquired with the samples in this form were used only to check the cross section at the peak of the Maxwellian velocity distribution (.0253 eV) where energy changes of the scattered neutron can be assumed to cancel. The 2200 m/sec cross section obtained in this way agreed very well with that obtained with the samples in forms (1) and (3).

The aluminum cans in form (3) had .02 in. walls and a .125 in. thick rim. The tungsten trioxide was pressed into the cans using a special die under 2 tons/sq in. pressure. Radiographs indicated that the samples were uniform within $\pm$ 5%. The weights of all the cans were adjusted to the same value (10 grams) and an empty can placed in the neutron beam was used to measure the capture rate in the aluminum. These data were used to correct the tungsten data for captures in aluminum.

The effect of scattering from aluminum on the tungsten capture rate was taken into account by adjusting the energy independent component of the tungsten trioxide scattering cross section in each case.

III. METHOD OF ANALYSIS

The equation which relates the capture rate in the i^{th} isotope to the cross section is given by:

$$C_i(t) = \epsilon_i s\phi(t)\,(1-e^{-N\sigma})\,\frac{a_i\sigma_{\gamma if}}{\sigma f_0} \qquad (1)$$

where:

ϵ_i = efficiency for detection of captures in isotope i

$\phi(t)$ = neutron flux in neutrons/cm^2

N = number of sample atoms/cm^2

σ = total cross section in cm^2

a_i = abundance of the i^{th} isotope

$\sigma_{\gamma i}$ = capture cross section of the i^{th} isotope

s = sample area in cm^2

f_0 = probability of capture of an incident neutron on the first interaction

f = total neutron capture probability.

If more than one isotope is present then $C = \Sigma_i C_i$. Solving for $\sigma_{\gamma i}$ in this sum we obtain:

$$\sigma_{\gamma i} = \left[\frac{C(t)\sigma f_0}{s\phi(t)(1-e^{-N\sigma})f} - \sum_{k\neq i} a_k \epsilon_k \sigma_{\gamma k} \right] (a_i \epsilon_i)^{-1} \qquad (2)$$

where C(t) is the number of capture counts observed at time t. The sum over the depleted isotopes in eq (2) corrects for captures in isotopes other than the enriched one. It should be noted in eq (2) that the $\sigma_{\gamma k}$ are in general unknown. Hence eq (2) must be solved by iteration employing a data set corresponding to each of the enriched isotopes. A computer code was used to solve eq (2) at each time point for the four tungsten isotopes and gold.

In the cases of natural tungsten and gold where the sum of the abundance weighted isotopic capture cross sections is being measured, eq (2) becomes:

$$\sigma_{\gamma} = \frac{C(t)\sigma f_0}{\epsilon(t)s\phi(t)(1-e^{-N\sigma})f} \qquad (3)$$

where ϵ (t) is the efficiency for detecting a capture in a natural sample given by:

$$\epsilon(t) = \frac{\Sigma_i \epsilon_i a_i \sigma_{\gamma i}(t)}{\Sigma_i a_i \sigma_{\gamma i}(t)}$$

The solution of eqs (2) and (3) requires a knowledge of the multiple scattering effect, i.e. f_0/f. The multiple scattering correction employed (See Appendix I) is a first order analytic calculation of the fraction f_1 of neutrons which capture after the first scattering collision. The scattering cross sections for tungsten were those calculated from the resonance parameters listed in (15).* The low energy scattering cross sections listed in (14) were used for oxygen and aluminum.

The calculation ignores energy changes of the scattered neutron and the effects of thermal motion of the scattering nucleus. These effects

*The low energy scattering cross sections listed in (15) seem to be in error.

are appreciable in the Lorentzian portion of the low energy resonances and hence no attempt was made to analyze the data in these regions.

The sample was considered to be an infinite slab which is justified by the large diameter-thickness ratios for the samples employed. The geometric series approximation $\frac{f_0}{f} = 1-\frac{f1}{f_0}$ was used as the correction for the total of all scattered neutron captures.

IV. EXPERIMENTAL RESULTS

The values obtained in this work for the thermal cross section of W^{182}, W^{183}, W^{184} and W^{186} are given in Table II. Also included are the values recommended in BNL 325 and the values calculated from the measured resonance parameters of the positive energy states.

TABLE II

Capture Cross Section at .0253 eV

Isotope	BNL 325	From Parameters	This Work
180	60.0 ± 60.0	a	
182	20.0 ± 2.0	13.5	20.7 ± 0.5
183	11.0 ± 1.0	9.5	10.0 ± 0.3
184	2.0 ± 0.3	0.76	1.7 ± 0.1
186	35.0 ± 3.0	44.2[b]	37.8 ± 1.2
Natural	19.2 ± 1.0	19.9	18.3 ± 0.5
Calculated[c]	17.5	18.2	18.3 ± 0.5[d]
Gold	98.8 ± 0.3	97.0	98.7 ± 1.8

a There are no reported parameters for W^{180}, however, a resonance at 15.8 eV has been assigned to this isotope[16]

b A recent infinite dilution resonance integral measurement on W^{186} [18] yielded a value 20% lower than that calculated from resonance parameters, which may indicate that the reported neutron width of the 18 eV level is too large.

c Calculated abundance-weighted cross section using 60 barns for W^{180}. The agreement between the measured and calculated natural cross section of this work is fortuitous.

The natural tungsten cross sections listed in Table II were obtained using the abundances listed in the Handbook of Physics and Chemistry.[17] The relative contribution of the various isotopes to the natural tungsten thermal cross section can be seen in Table III.

TABLE III

Isotope	Natural Abundance	Thermal Capture Cross Section (barns)	Thermal Contribution (barns)	% of Total
180	.00126	(60.0 ± 60.0)[a]	0.076 ± 0.076	0.4 ± 0.4
182	.2631	20.7 ± 0.5	5.45 ± 0.13	29.8 ± 0.7
183	.1428	10.0 ± 0.3	1.42 ± 0.04	7.8 ± 0.2
184	.3064	1.7 ± 0.1	0.52 ± 0.03	2.8 ± 0.2
186	.2864	37.8 ± 1.2	10.83 ± 0.34	59.2 ± 1.9

a BNL 325 value used.

The error sources involved in the cross section determination fall into three classes. These are:(1) errors which affect the normalization, (2) errors which affect the energy scale, and (3) errors which affect the shape of the curve relative to the normalization point. Some of the errors involved are not analytic in nature, and hence only subjective estimates can be given. Table IV enumerates all known sources of errors and their estimated magnitude for each of the isotopes.

TABLE IV

CLASS (1) ERRORS IN NORMALIZATION

	Error Type	% Error	
		Tungsten $^{182, 183, 184, 186}$	Gold
1-1	Parameters of flux calibration resonances (4.15 eV in W^{182} and 4.906 eV in Au^{187})	<0.01	<0.01
1-2	Resolution correction to flux calibration.	0.04	<0.01
1-3	Analyzer dead time correction	<0.01	<0.01
1-4	Statistical errors in calibration interval	0.7	0.6
1-5	Background subtraction in calibration	<0.01	<0.01
1-6	Purity and deviation from formula weight	1.0	0.1
1-7	Extrapolation to zero bias	2.0[a]	0
1-8	Gain shift after normalization	0.8	0.7
1-9	Gamma attenuation in sample	0-1	0
1-10	Error in flux shape exponent	0.9	1.7

CLASS (2) ERRORS IN ENERGY SCALE

		All Isotopes
2-1	Flight path length	0.1
2-2	Frequency or analyzer clock	0.2
2-3	Analyzer start time	1.0-0.02

CLASS (3) SHAPE ERRORS

		W^{182}	W^{183}	W^{184}	W^{186}	Au^{197}
3-1	Scattering cross section used in multiple scattering calculation	0.5	0.3	0.8	0.3	0.02
3-2	Assumption of no energy change in scattered neutrons, infinite slab approximation and isotropic scattering approximation in multiple scattering calculation	<0.1[b]	<0.1	<0.1	<0.1	<0.01
3-5	Effect of WO_3 on aluminum capture	0.01	0.3	0.6	<0.01	0
3-6	Isotopic abundancies	0.5	0.5	0.5	0.5	0
3-7	Subtraction of captures due to contaminating isotopes[c]	0.1	0.6	3.8	0.02	0
3-8	Statistical uncertainty in points	.2-3.	.1-5.	1.-10.	.1-3.	.1-3.
3-9	Boron flux shape	1.0	1.0	1.0	1.0	1.0
3-10	Analyzer dead time correction	<0.01	<0.01	<0.01	<0.01	<0.01
3-11	Insensitivity to gamma spectrum changes	0.1	0.1	0.1	0.1	0.1
3-12	Flux-capture flight path differences	<0.7	<0.7	<0.7	<0.7	<0.7
3-13	Background subtraction[d]	<0.3	1.3-5.	2.-11.	<0.2	<0.3
3-14	Error in flux shape exponent[e]	<0.9	<0.9	<0.9	<0.9	<0.9

a 0. for W^{182}

b These limits might be exceeded in the 5 to 7.5 eV region in W^{182} and the 9 to 10 eV region in W^{183} due to the large energy loss in oxygen scattering which might scatter neutrons into the low energy resonances in these isotopes.

c These errors are exceeded near the low energy resonances.

d Errors due to backgrounds are largest from 1 to 10 eV, and are very much smaller at other energies.

e 1 to 10 eV only.

The cross section data shown in Fig. 13 through 18 represent the weighted average of data acquired on six different dates. In each case the flux shape and backgrounds as well as flux calibration and pulse height distribution data were taken. In this way the effects of changes in the apparatus between data runs were eliminated.

The time of flight data, after being corrected for analyzer dead time and backgrounds, were grouped and interpolated on a set of energy points. These energy points correspond to the data points shown in the figures. In all cases the neutron energy resolution width is much smaller than the energy difference between the points shown. Equation (2) was solved for each of these energy groups, and hence contains a "resolution" error which becomes appreciable when the flux shape or cross section varies rapidly with energy. This occurs only in the low energy resonances, and since, as explained earlier, the data in the vicinity of these resonances are unreliable, the data points in these energy regions were omitted from the figures.

The measured W^{182} cross section shown in Fig. 13 is significantly higher than that calculated from positive energy resonances including a statistical term for the unresolved region. The discrepancy can be accounted for by postulating a 1/v contribution from negative energy levels. The choice of parameters for such a level is arbitrary with the sole restriction that the "resonance" energy be much less than -10 eV in order that its contribution vary essentially as 1/v in the region of the measurement. Since W^{182} is an even-even nucleus, g = 1. The best choice of Γ_γ is the average radiation width of the positive energy levels, i.e. 57 meV. The average reduced neutron width of 20 $meV/eV^{1/2}$ was chosen which yields a resonant energy of -30.7 eV, which is sufficiently small to yield a 1/v contribution. The dashed curve shown in Fig. 13 was obtained by adding this contribution to that of the positive energy levels. There is some indication that the negative energy contribution does not quite vary as 1/v due to the systematic deviation near 10 eV. No attempt was mad

to improve the fit by the inclusion of a non 1/v negative energy contribution due to the doubtful significance of the deviation.

The W^{183} cross section shown in Fig. 14 is slightly below the calculated curve by an amount which exceeds the errors in this measurement. The discrepancy is thought to be due to errors in the resonance parameters used.

The W^{184} data points shown in Fig. 15 lie well above the calculated curve which again indicates a negative energy contribution. The "parameters" for the negative energy level obtained in the same fashion as those for W^{182} are: g=1, $\Gamma_\gamma = 57$ meV, $\Gamma_n^o = 48.4$ meV/eV$^{1/2}$, $E_o = -110$ eV. Again there is an indication of a non 1/v negative energy contribution, but the significance of this deviation is again doubtful.

Three calculated cross section curves for W^{186} are shown in Fig. 16. The upper one was obtained from the parameters listed in Ref. (15) and the lower one from those listed in Ref. (19). It can be seen that the data points lie at an intermediate position. Since the cross section is dominated by the 18.8 eV level, the error can probably be ascribed to the $\Gamma_n\Gamma_\gamma$ product for this level which is 1.413×10^{-2} eV^2 for the measured curve as opposed to 1.648×10^{-2} eV^2 for the upper calculated curve and 1.197×10^{-2} eV^2 for the lower one. Since the radiation width used in the upper curve is probably more reliable than the neutron width, the latter quantity was adjusted to force agreement at thermal energy. The result is the solid curve which is in good agreement with the data throughout the measured energy interval.

The measured natural tungsten cross section is shown in Fig. 17 along with a calculation from the positive energy parameters listed in Ref. (15). Also shown is the calculated cross section including the two negative energy levels evaluated earlier as well as the adjusted neutron width of the 18.8 eV level in W^{186}. These two curves agree below 1 eV due to a fortuitous cancellation of the errors in the isotopic cross sections calculated from the positive energy parameters. The natural tungsten

cross section obtained by abundance weighting the measured isotopic cross sections are also shown. The natural tungsten cross section obtained in this way is in very good agreement with the measured cross section of natural tungsten except in the region near 10 eV where statistical uncertainties are appreciable.

Finally in Fig. 18 the measured gold cross section is compared to that obtained from the best set of resonance parameters. It can be seen that the agreement is very good throughout the energy region investigated.

V. CONCLUSIONS

The magnitudes of the 2200 m/sec cross sections for W^{182}, W^{183}, W^{184}, and W^{186} have been obtained with appreciably smaller errors than have been previously reported. The capture cross section shapes reported here for the tungsten isotopes are the first in this energy region, and illustrate the utility of the technique as a check on measured low energy resonance parameters and in the determination of negative energy level effects. The agreement between the natural tungsten cross section as measured directly with that obtained from isotopic cross sections, as well as the agreement of the gold cross section with the best values available lend support to the belief that the techniques used here will be of value in obtaining accurate low energy capture cross sections for most of the isotopes of interest in reactor physics.

We would like to acknowledge the assistance of J. R. Beyster, J. C. Young, and J. Neill in the low energy flux shape measurements and of Floyd Bell in apparatus fabrication.

REFERENCES

1. Hughes, D. J., Pile Neutron Research, Addison-Wesley Publishing Co., Cambridge, Mass.

2. Lyon, W. S., "Reactor Neutron Activation Cross Sections for a Number of Elements," Nuc. Sci. and Eng. 8, (1960), pp. 378-380.

3. Schmunk, R. E., Randolph, P. D. and R. M. Brugger, "Total Cross Sections of Ti, U, Y, Ta,and W," Nuc. Sci. and Eng. 7, (1960), pp. 193-197.

4. Carter, R. S., Palevsky,H., Myers, V.W.and D. J. Hughes, "Thermal Neutron Absorption Cross Sections of Boron and Gold," Phys. Rev., 92, No. 2 (1953) pp. 716-721.

5. Haddad, E., Walton, R. B., Friesenhahn, S. J., and W. M. Lopez, Nuc. Sci. and Methods, 31 (1964), pp. 125-138.

6. Groshev, L. V., Demidov, A. M., Lutsenko, V. N., and V. I. Pelekhov, Atlas of Gamma Ray Spectra from Radiative Capture of Thermal Neutrons, Pergamon Press, New York, pp. 160, 174.

7. Nuclear Data Sheets, National Academy of Sciences--National Research Council.

8. Barrall, R. C., and W. M. McElroy, "Neutron Flux Spectra Determination by Foil Activation," AFWL-TR-65-34 Vol. II.

9. Julien, J., et al., "Détermination du Spin et des Paramètres des Résonances pour ^{197}Au + n de 10 eV à 1000 eV," (to be published).

10. Garrison, J. D. and B. W. Roos, "Fission Product Capture Cross Sections," Nuc. Sci. and Eng. 12 (1962), pp. 115-134.

11. Seth, D. J., Zimmerman, B. L., and R. C. Garth, Phys. Rev., 110 (1958), pp. 692-700.

12. Fröhner, F. H., and E. Haddad, "Analysis of Neutron Capture Data in the Resonance Region," Nuc. Phys. 31 (1965), 129.

13. Brother Austin Bernabie, F.S.C., "The Effects of Crystalline Binding on the Doppler Broadening of a Neutron Resonance," BNL 860 (T-344).

14. Hughes, D. J., and B. B. Schwartz, BNL 325, 2nd Ed. (1958), p. 61.

15. Joanou, G. D., and C. A. Stevens, "Neutron Cross Sections for Tungsten Isotopes," NASA-CR-54261.

16. Russell, J. E., Hockenbury, B. W., and B. C. Block, "Neutron Capture Measurements on the Isotopes of Tungsten," WASH 1046 p. 104.

17. Handbook of Physics and Chemistry, The Chemical Rubber Publishing Company, Cleveland, Ohio.

18. Shook, D., and D. Bogart, "Effective Resonance Integrals of Separated Tungsten Isotopes," Transactions of the American Nuclear Society, June 21-25, 1965, Vol. 8, No. 1, pp. 284-285.

19. Hughes, D., J., Magurno, B. A., and M. K. Brussel, BNL 325, Supp. #1, 2nd Ed., p. 36.

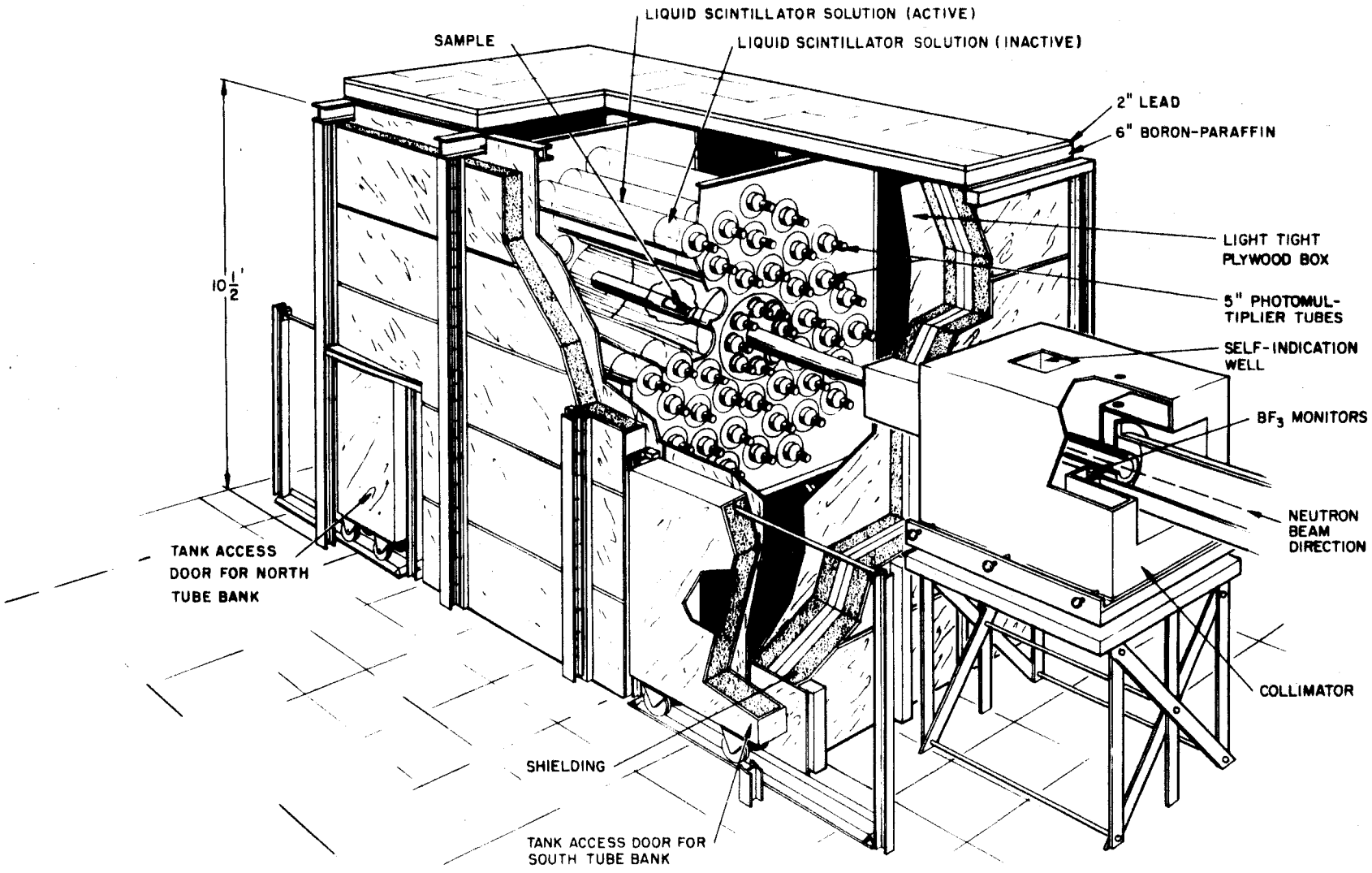

Fig. 1--View of large liquid scintillator showing the associated shielding and collimation.

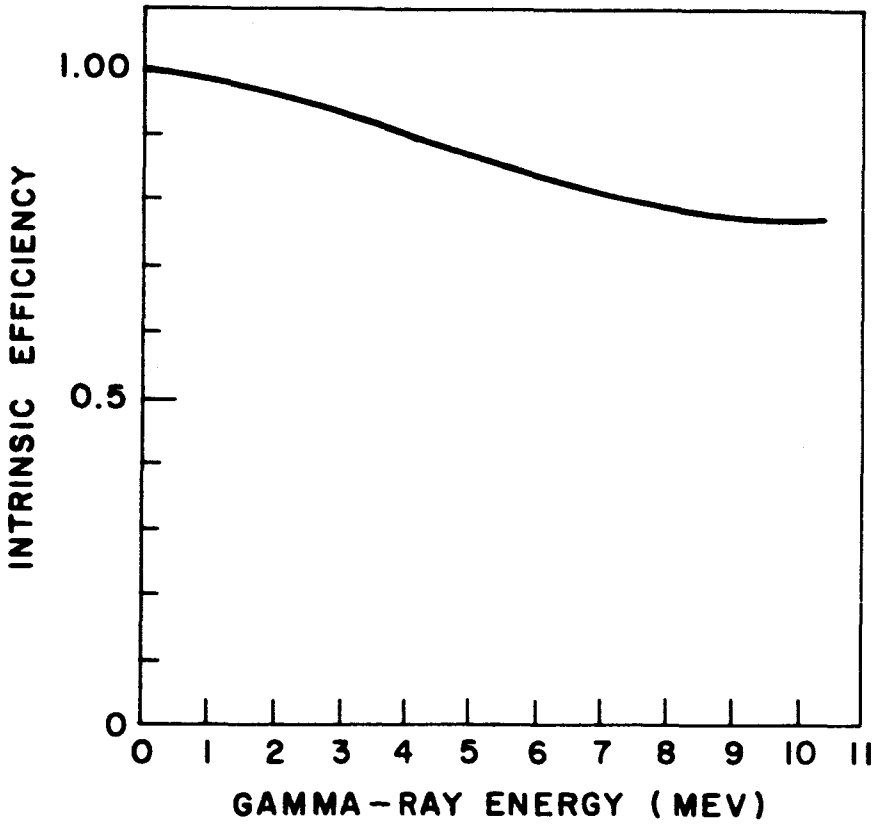

Fig. 2--Calculated first interaction probability for a single gamma to interact before escaping the large liquid scintillator.

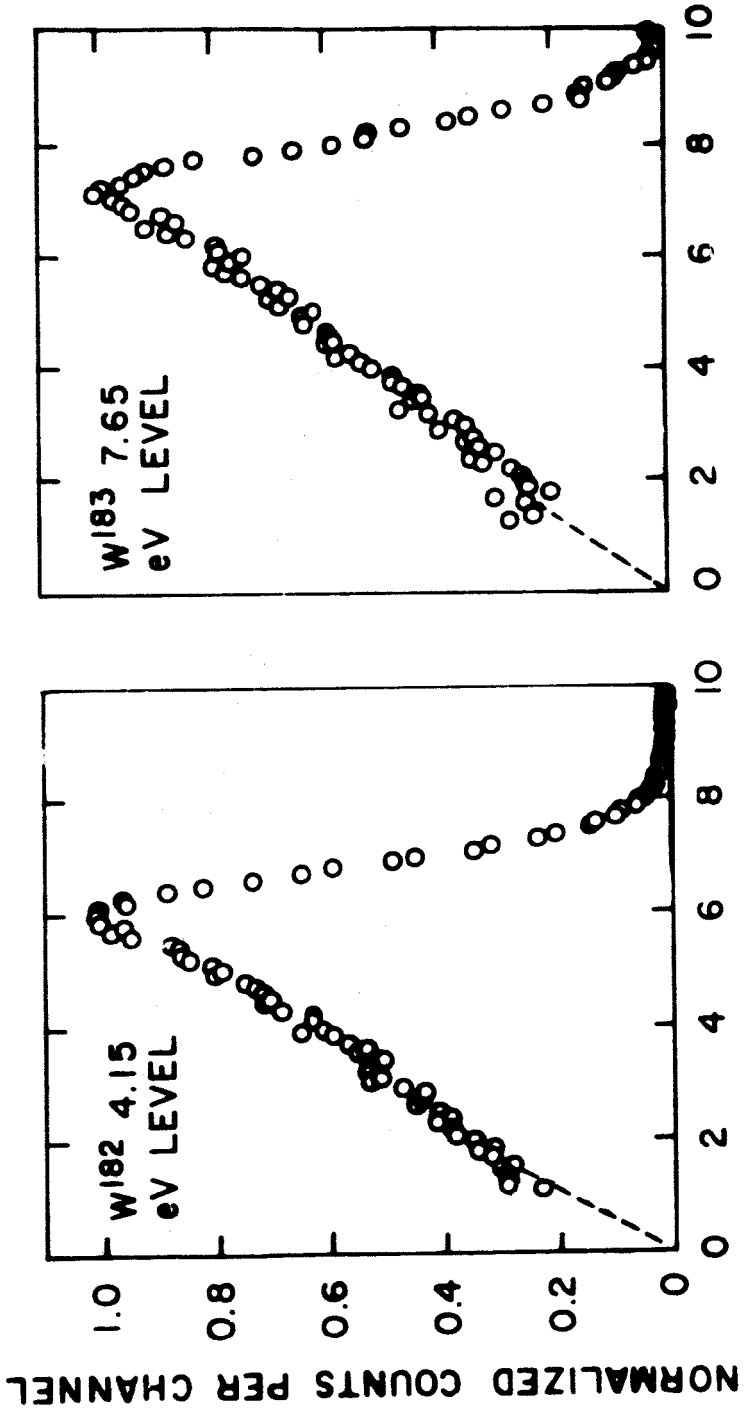

Fig. 3--Pulse height distributions due to captures in W^{182} and W^{183}.

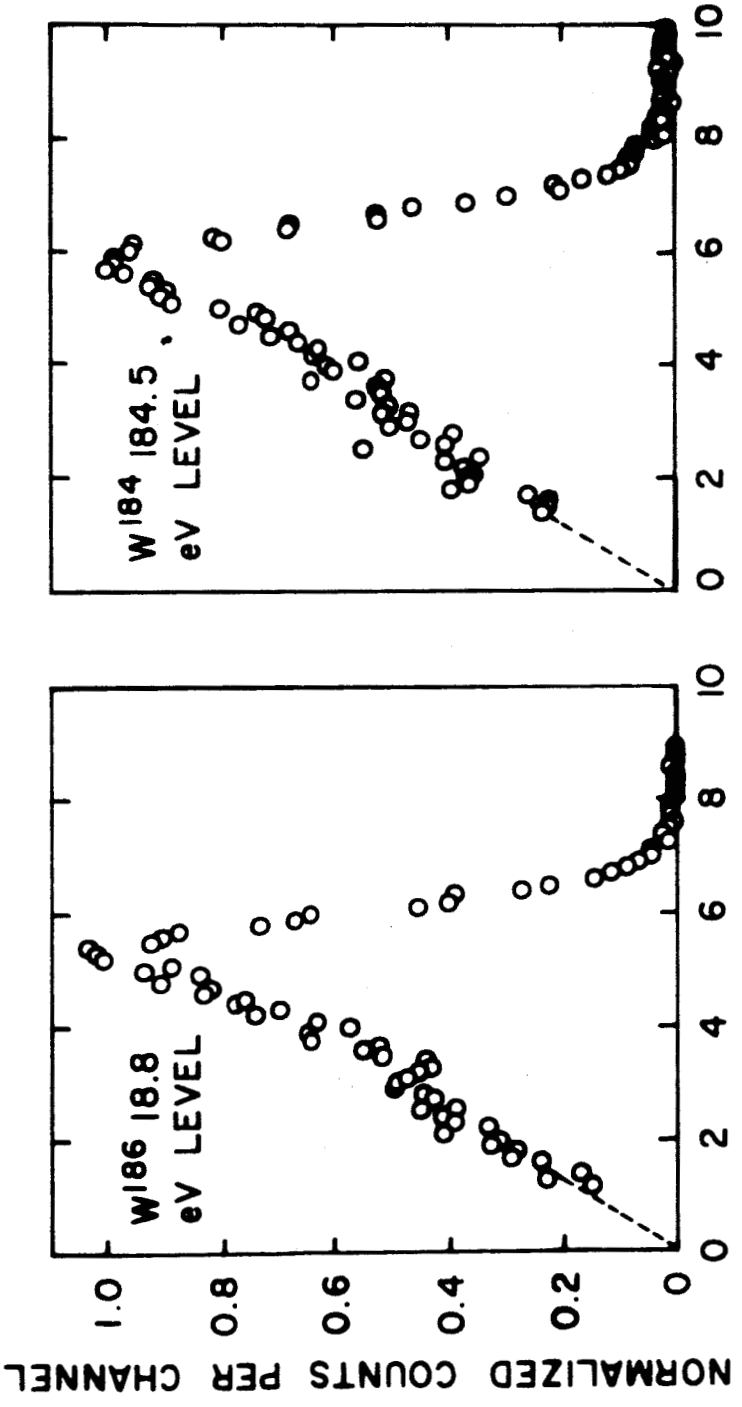

Fig. 4--Pulse height distributions due to captures in W^{184} and W^{186}.

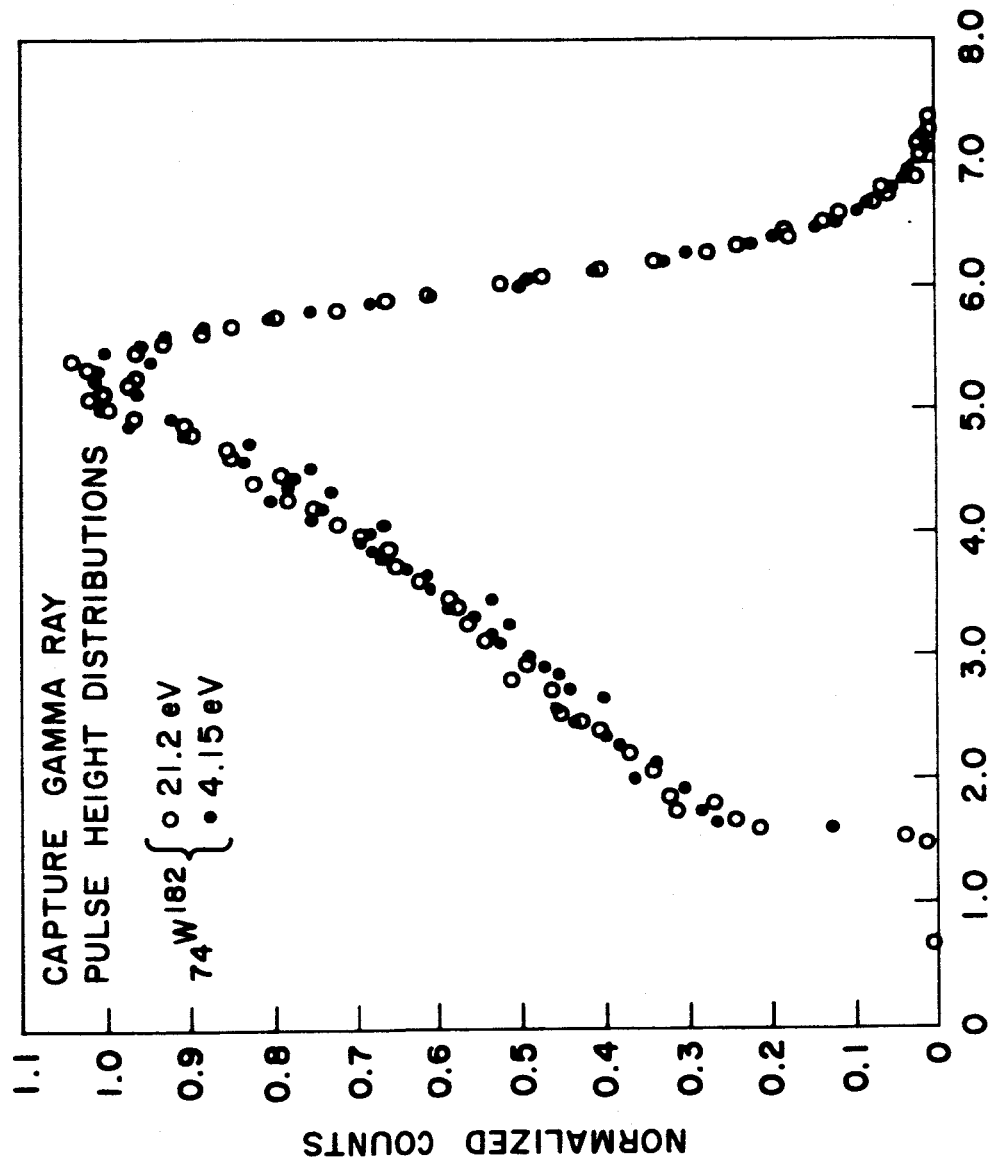

Fig. 5--Comparison of capture gamma ray pulse height distributions obtained from the 4.15 and 21.2 eV levels in W^{182}.

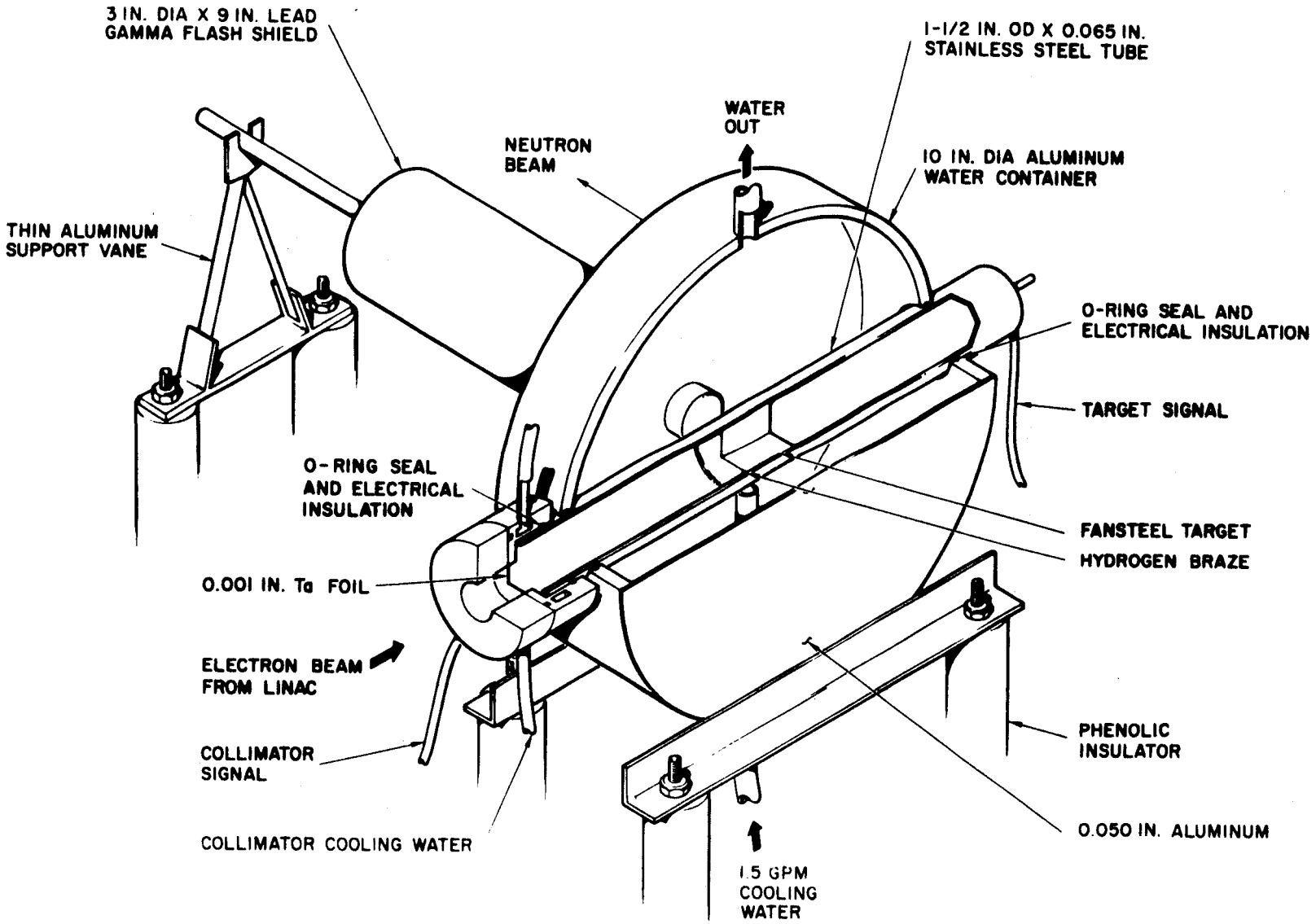

Fig. 6--Cross sectional view of electron target and moderator assembly.

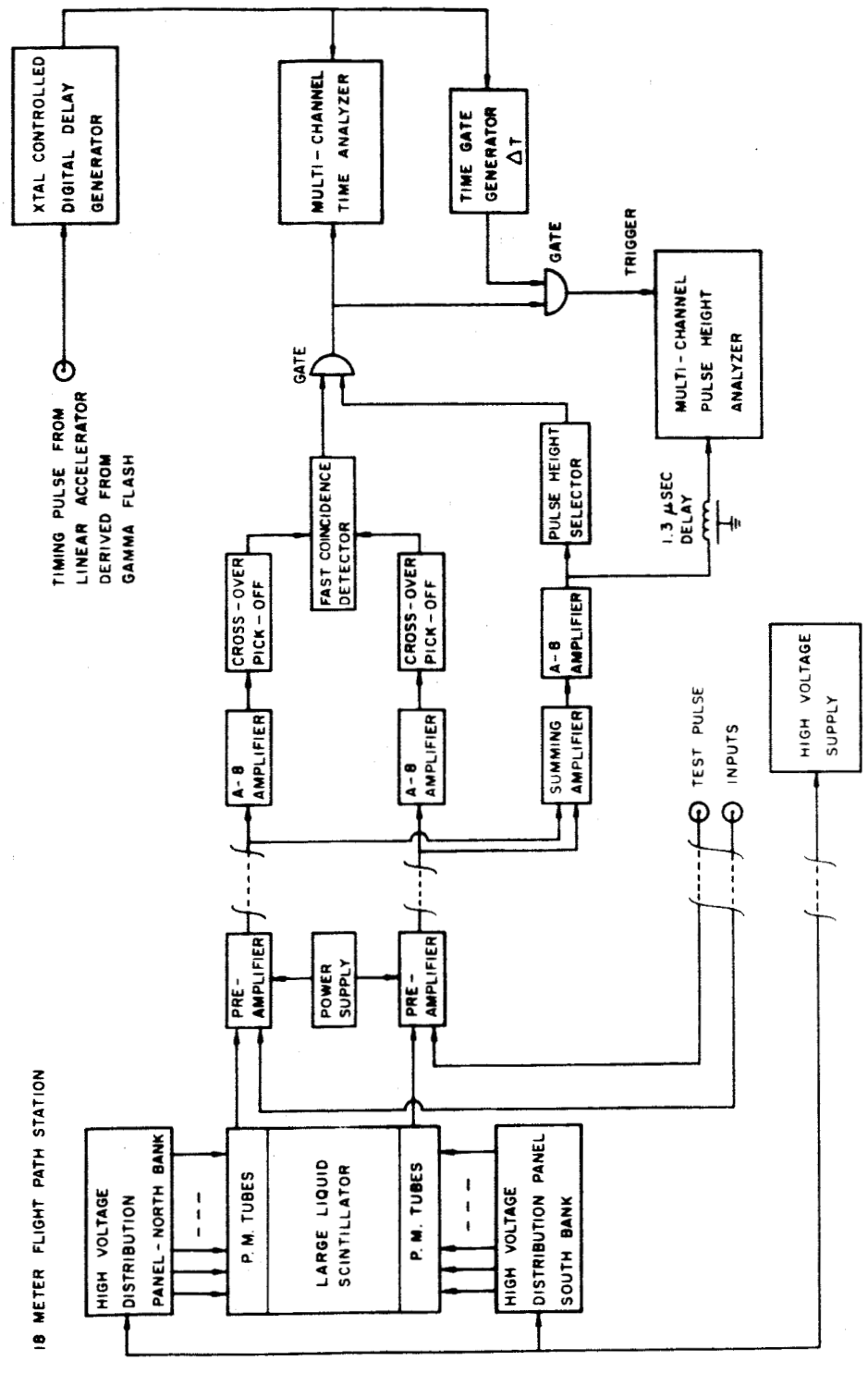

Fig. 7--Schematic of electronic configuration used in time-of-flight and pulse height data acquisition.

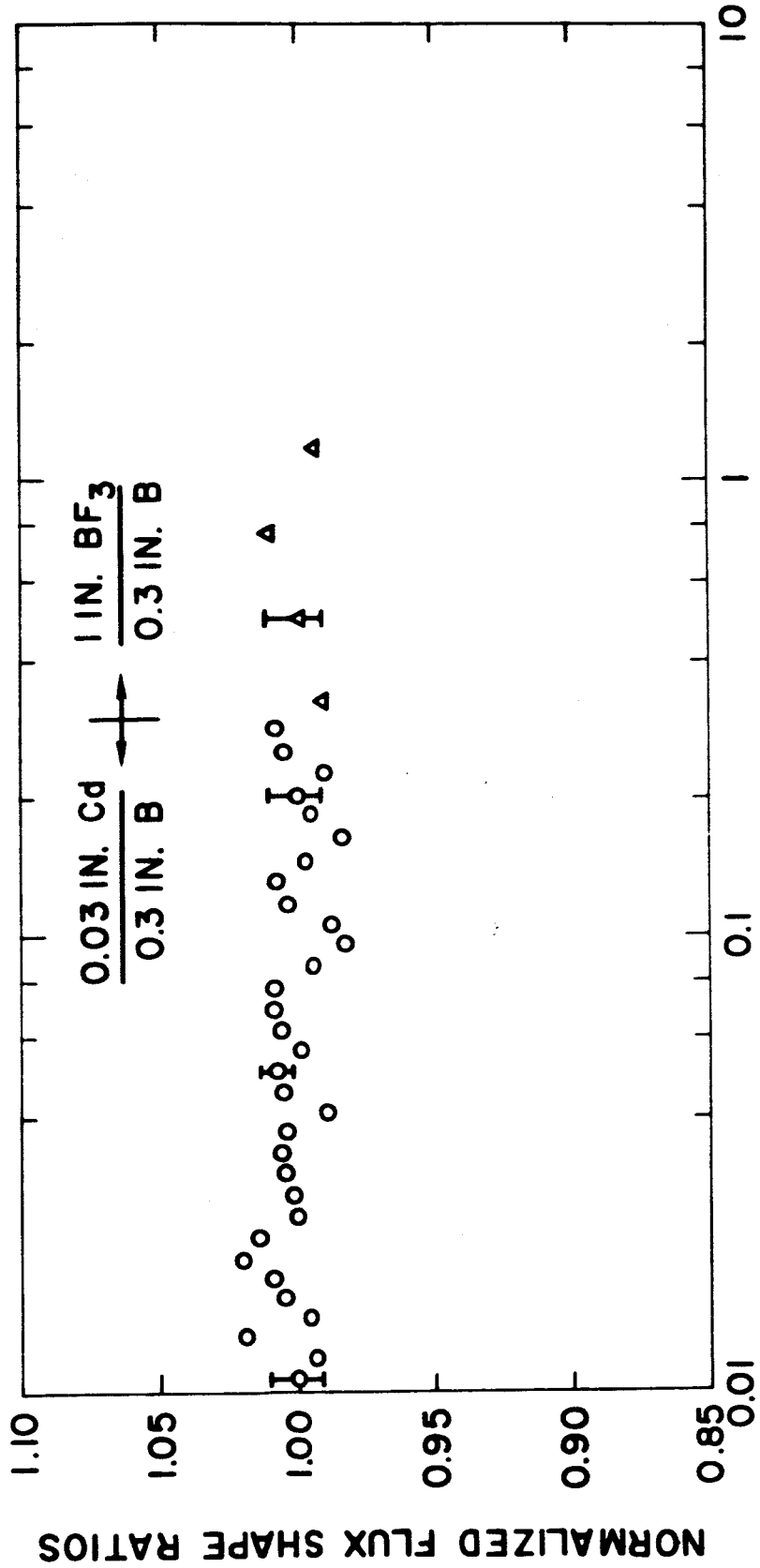

Fig. 8--Flux shape comparisons using thick boron slab and cadmium samples and a thin BF_3 tube with a 1/v resonance.

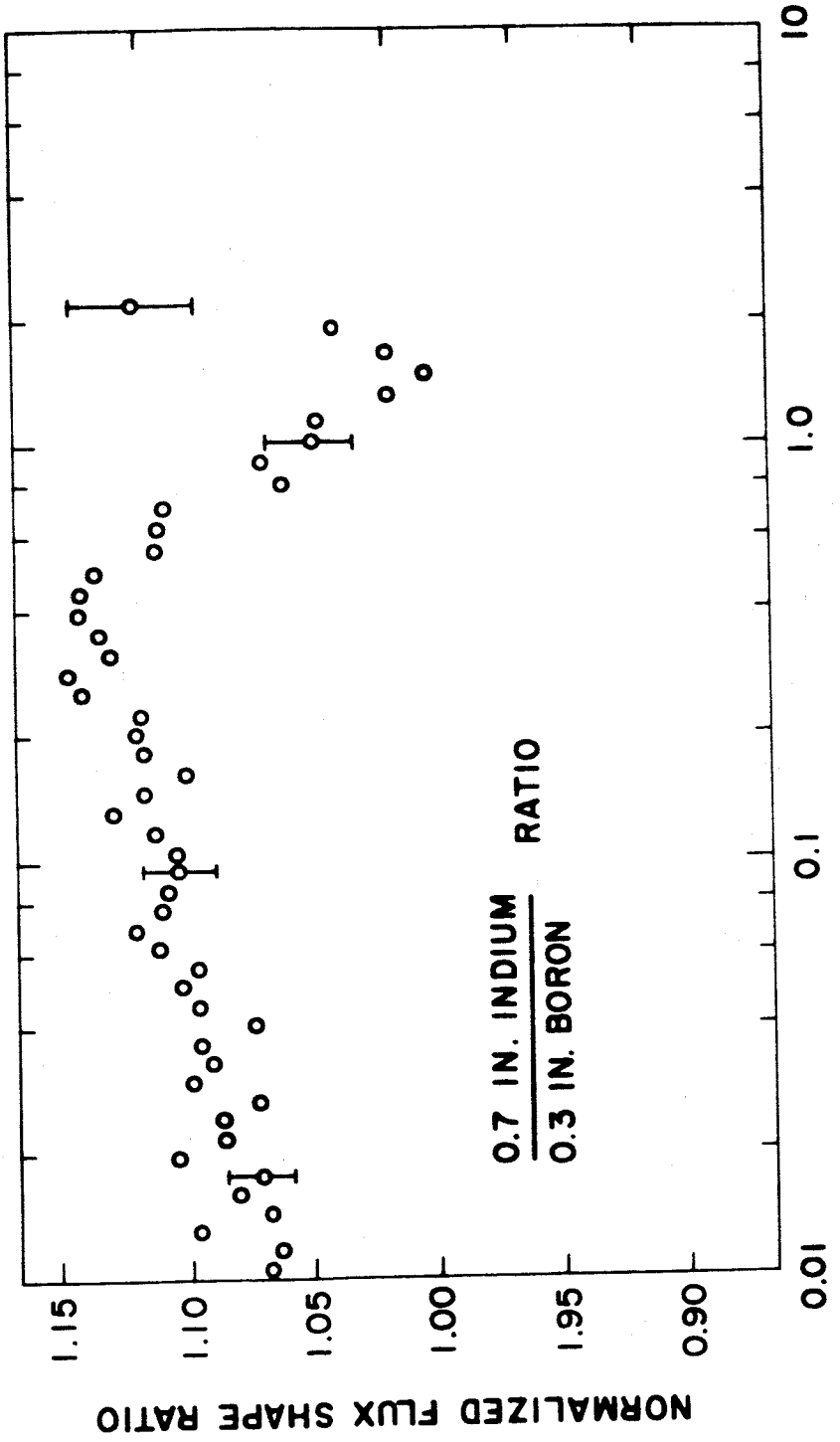

Fig. 9--Comparison of flux shapes measured with thick indium and boron slab samples.

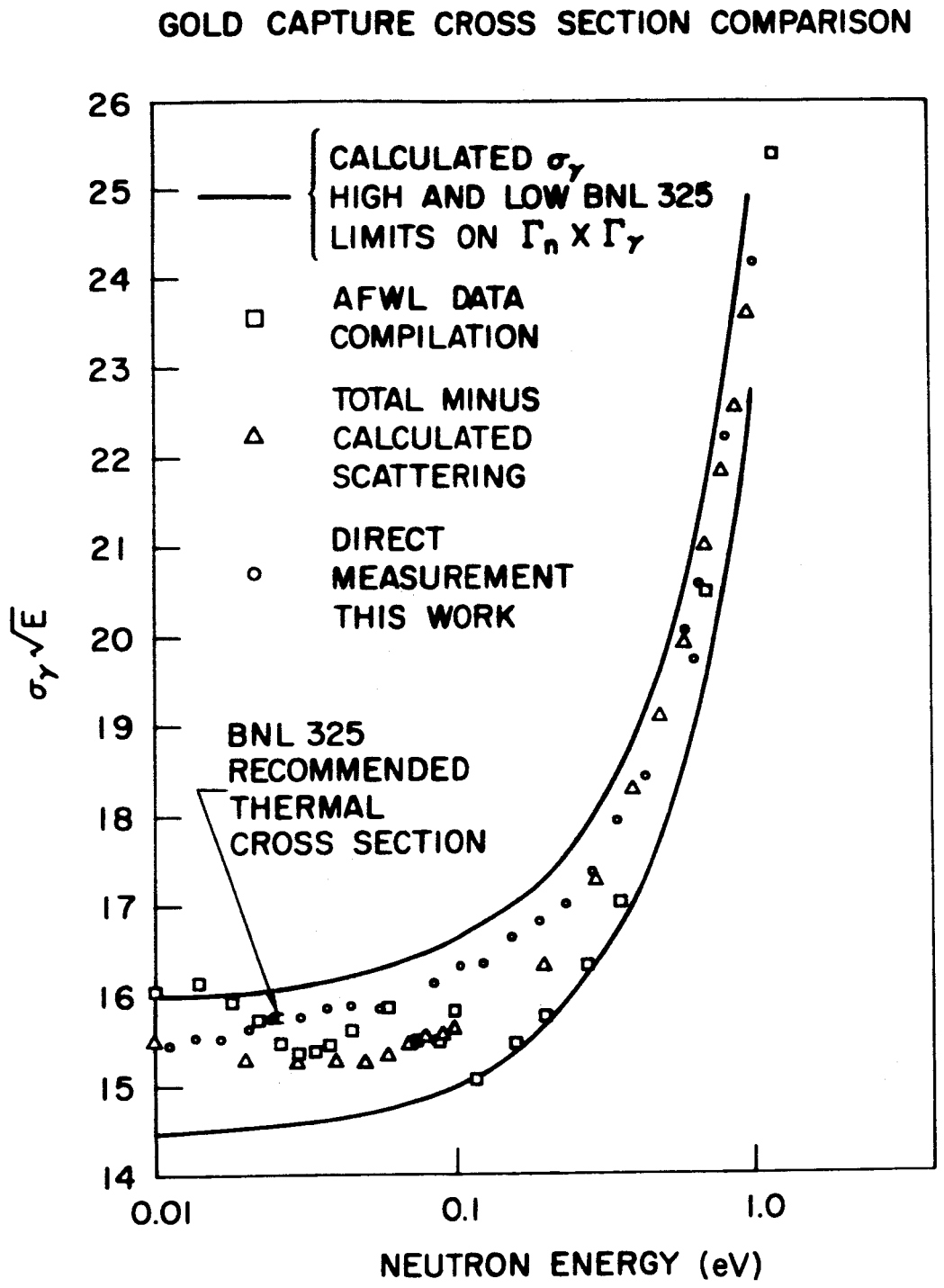

Fig. 10--Low energy gold cross sections obtained from various sources.

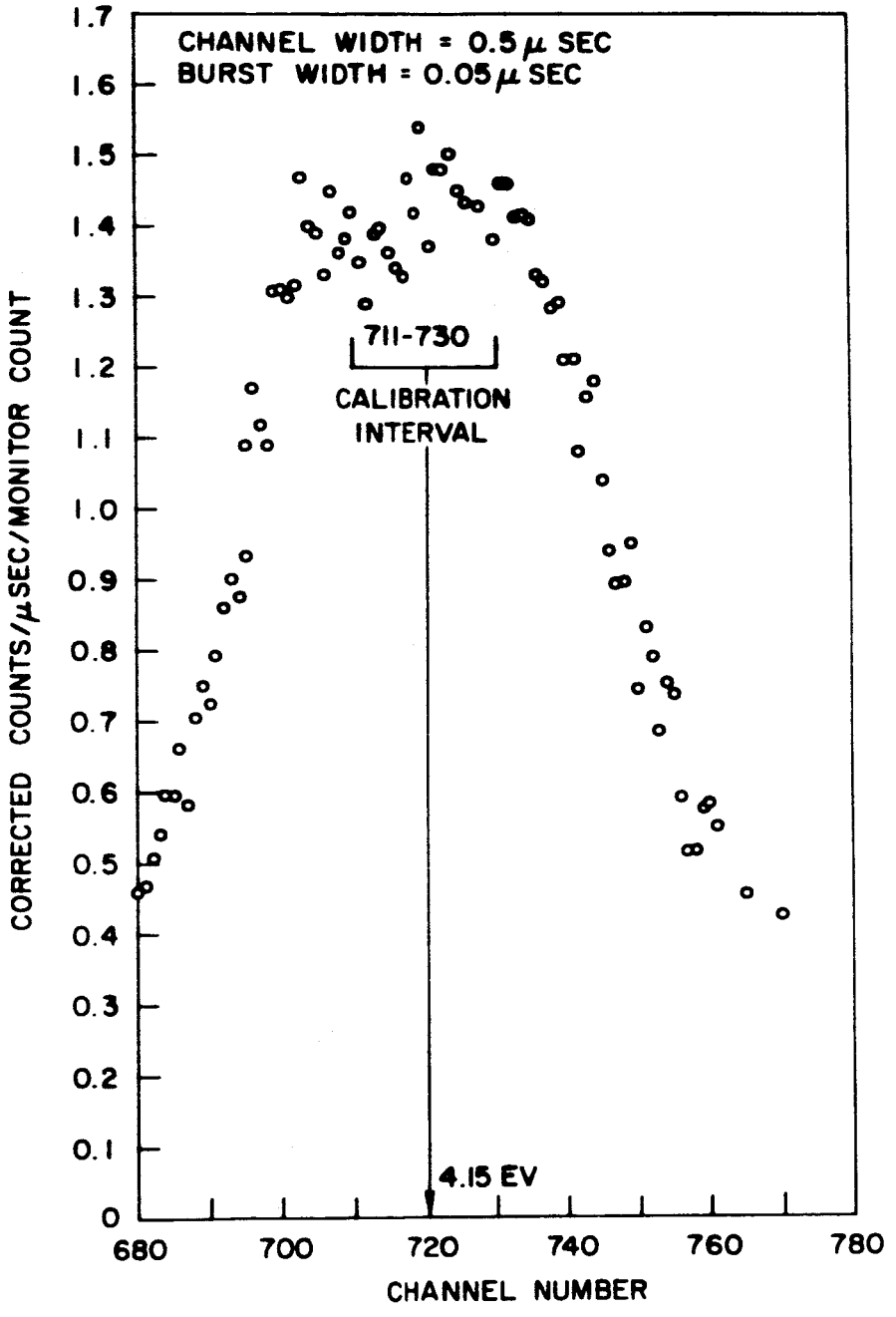

Fig. 11--Flux calibration data using the 4.15 eV resonance in W^{182}. The sample is .01 inch natural tungsten.

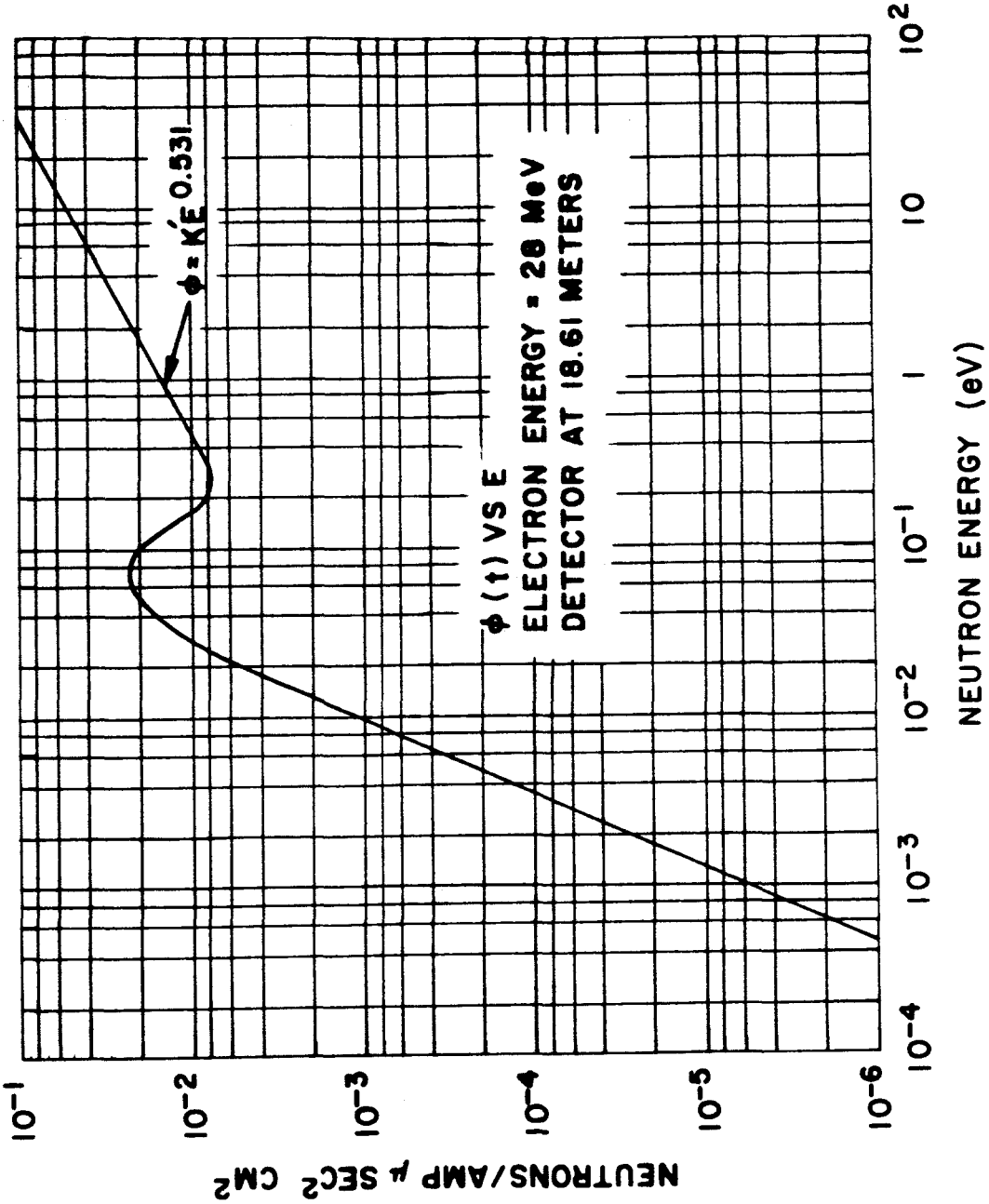

Fig. 12--Absolute neutron flux as a function of time.

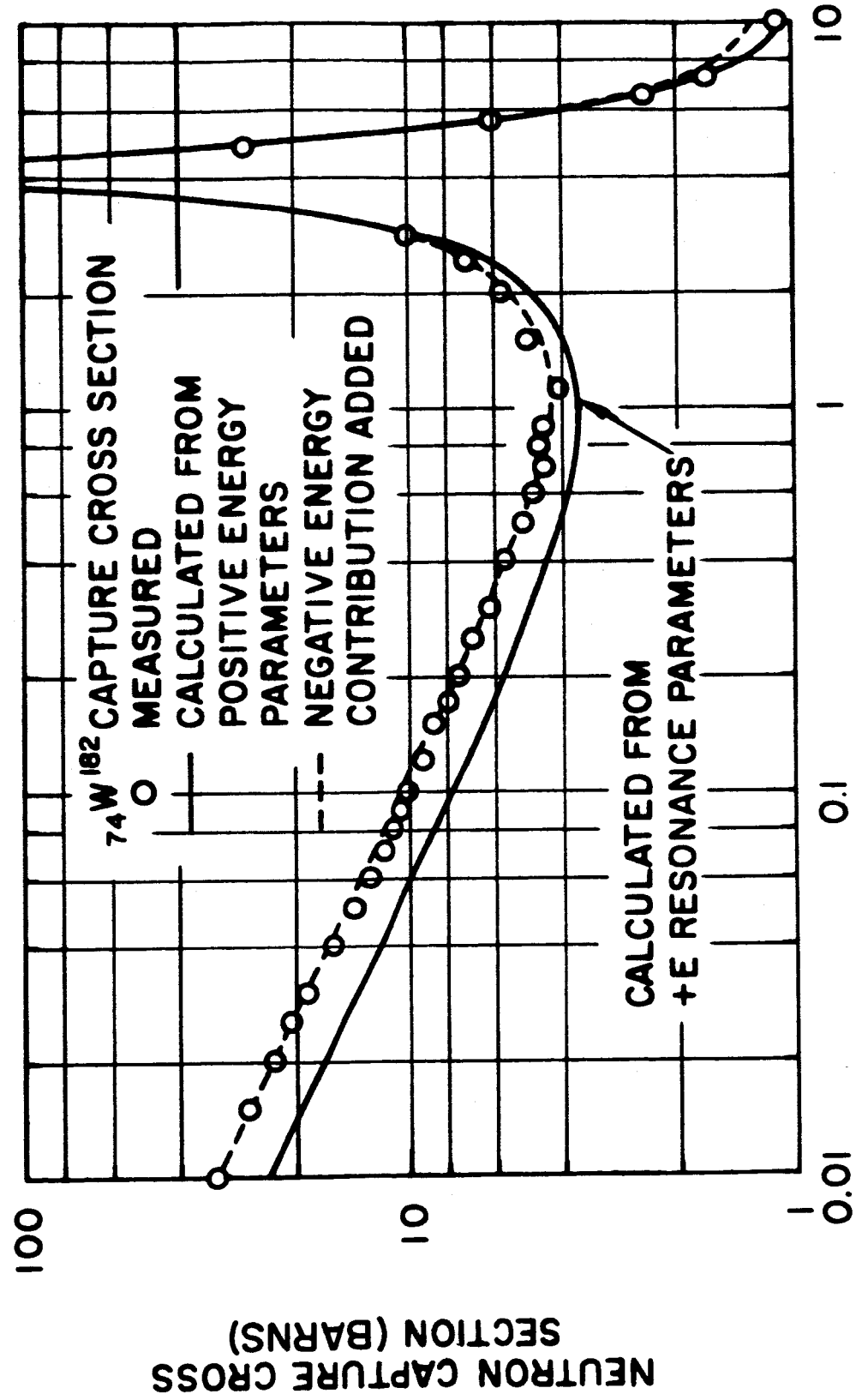

Fig. 13--Tungsten 182 cross section.

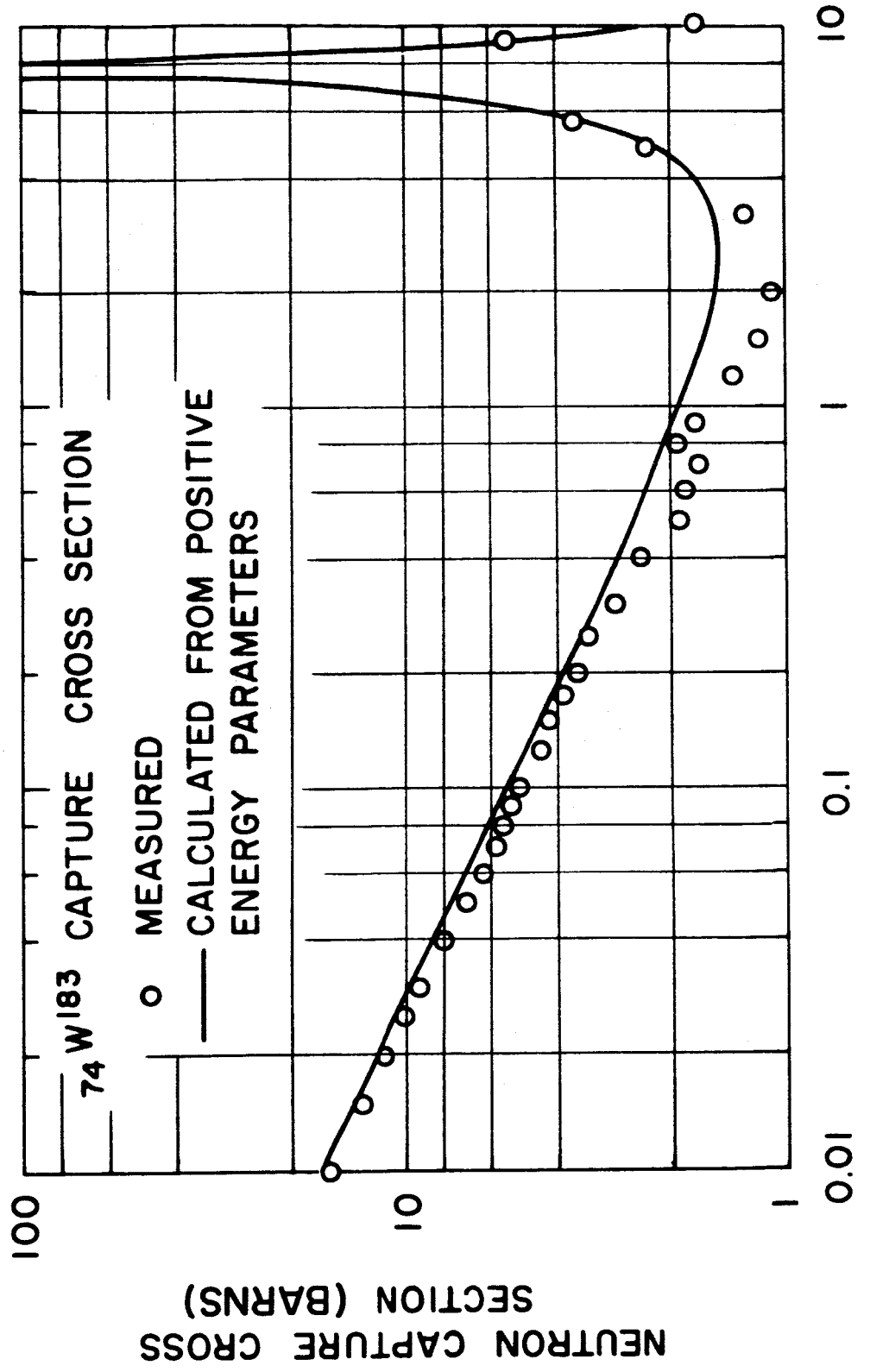

Fig. 14--Tungsten 183 cross section.

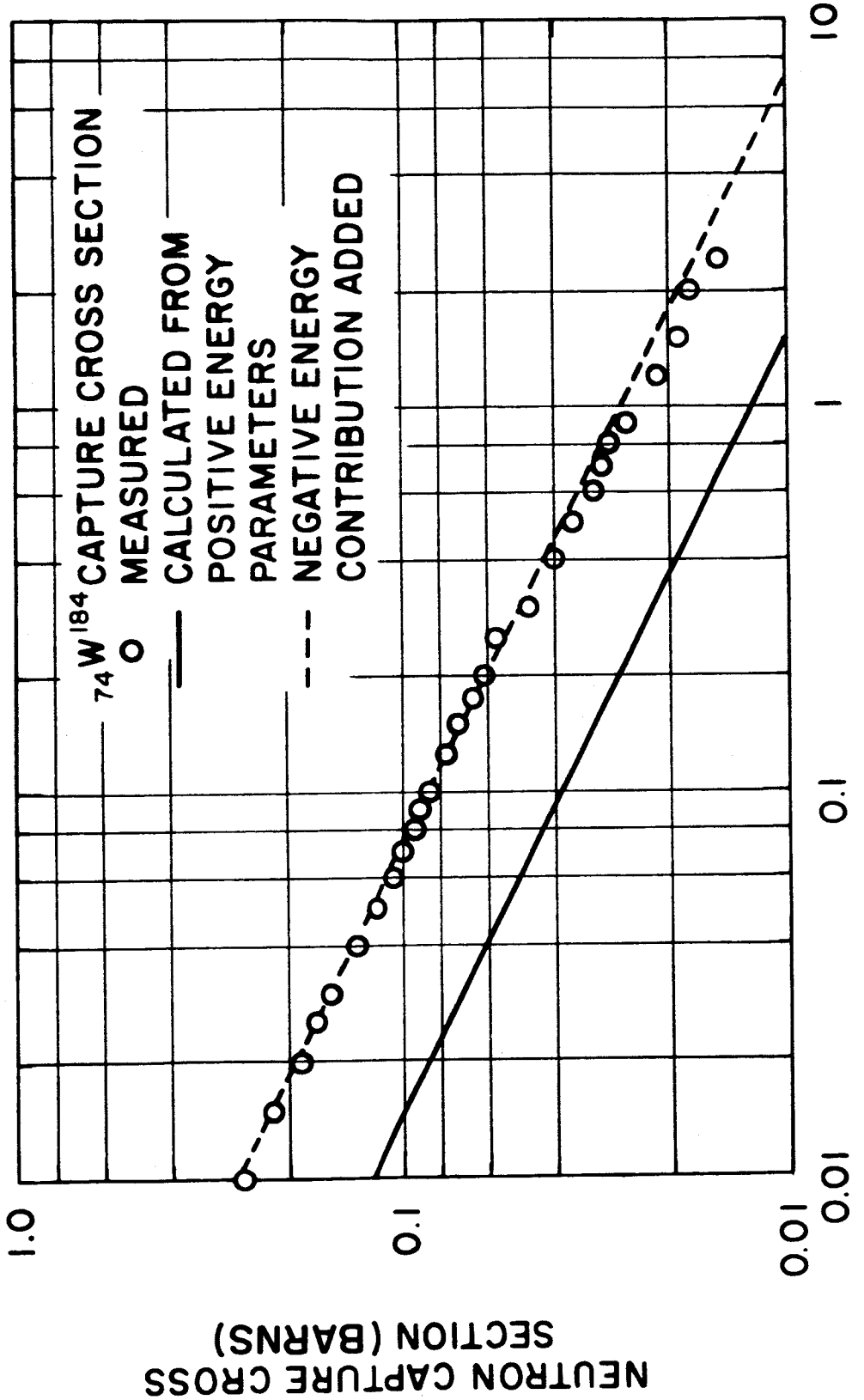

Fig. 15--Tungsten 184 cross section.

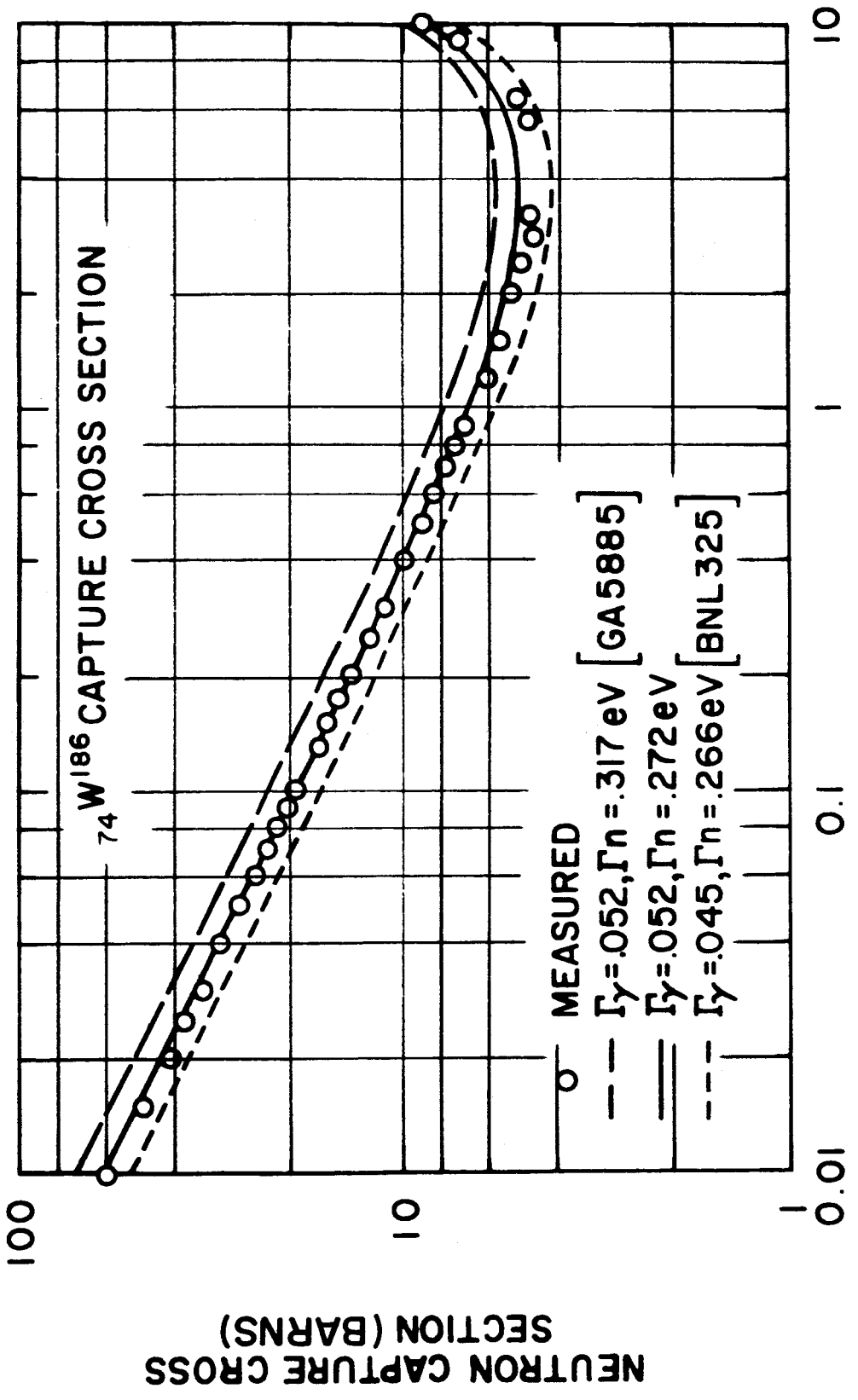

Fig. 16--Tungsten 186 cross section.

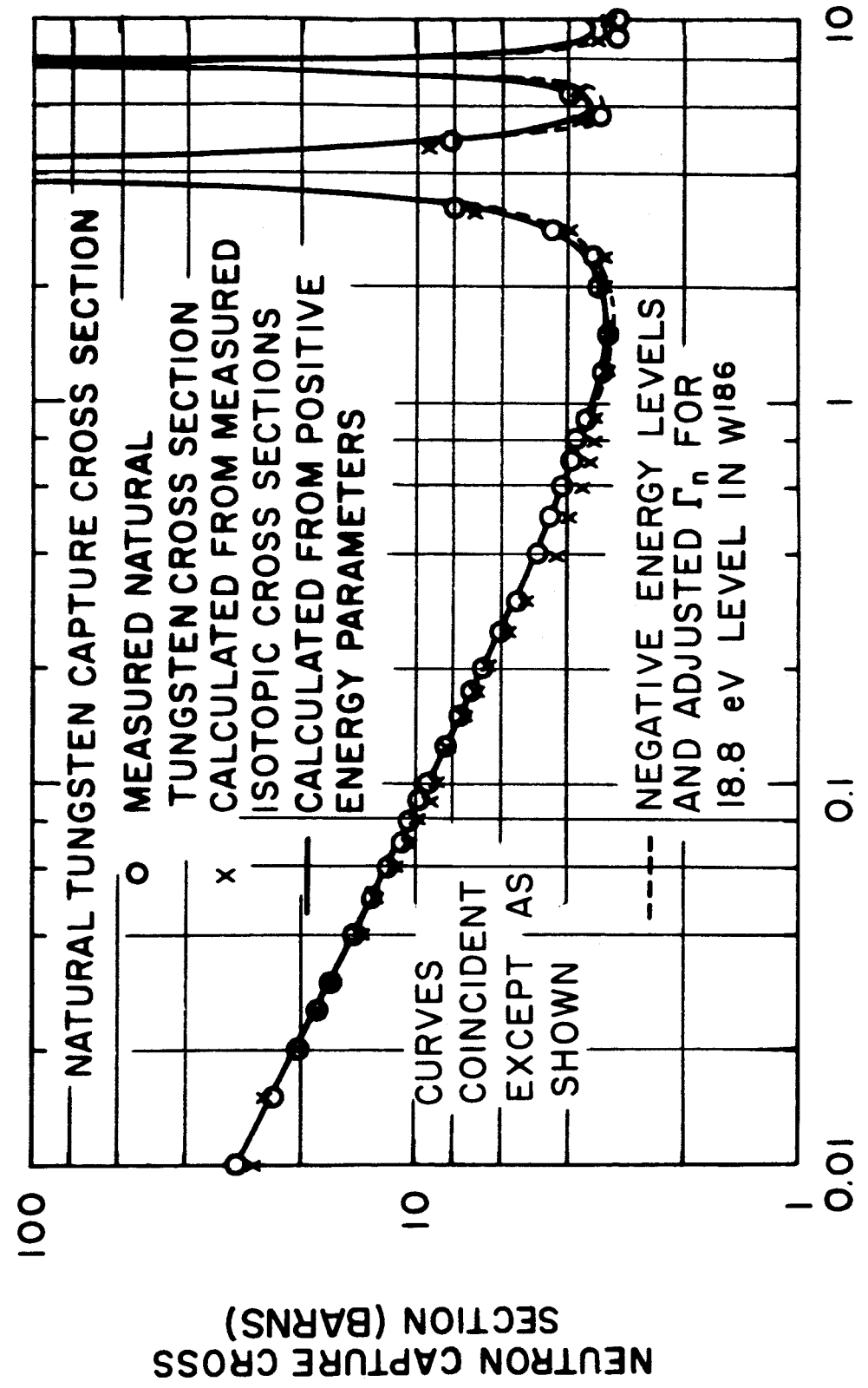

Fig. 17--Natural tungsten cross section.

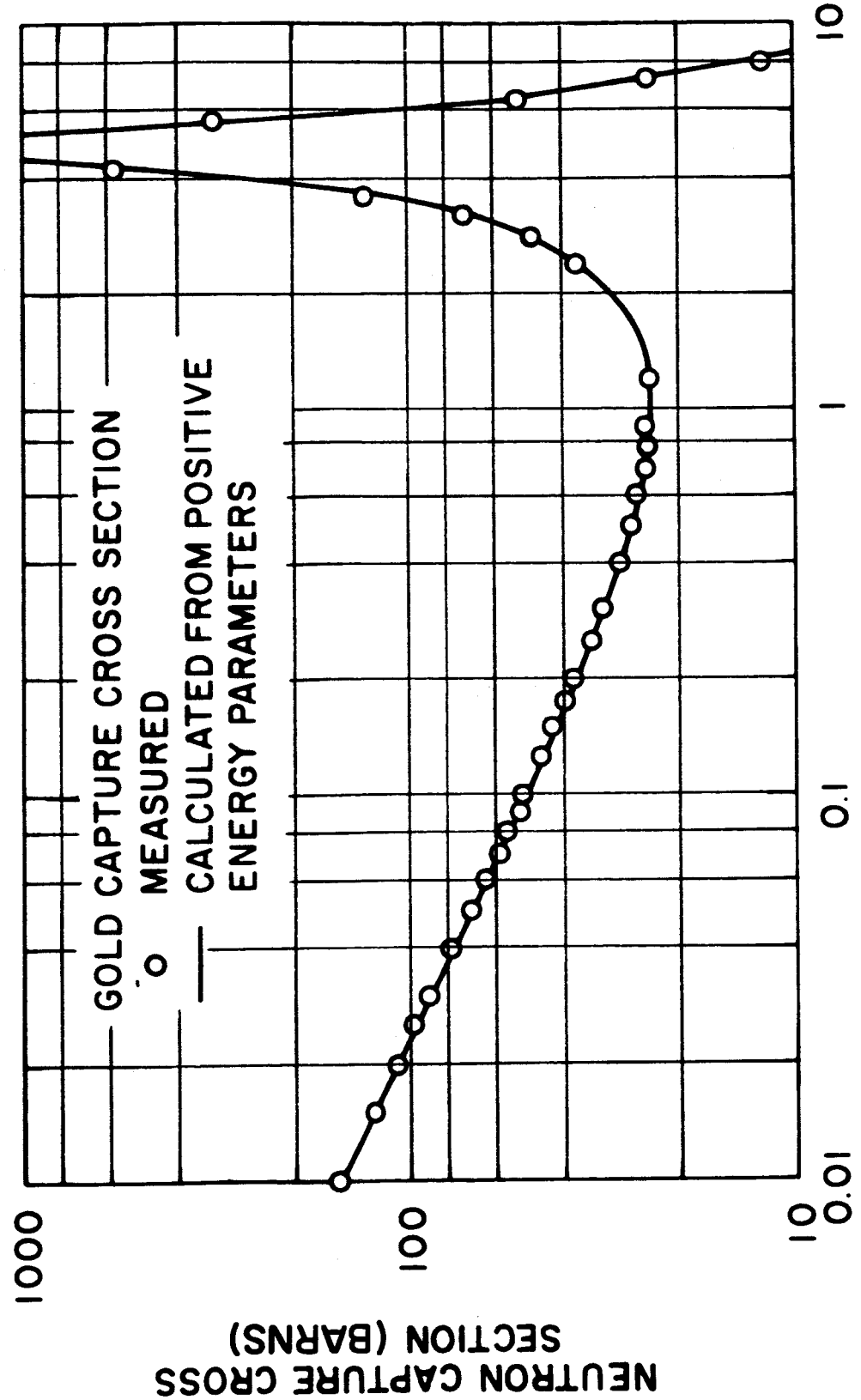

Fig. 18--Gold cross section.

Appendix I

MULTIPLE SCATTERING CORRECTION

Consider the case of capture after 0 or 1 scattering collisions, for which the probabilities are f_0 and f_1.

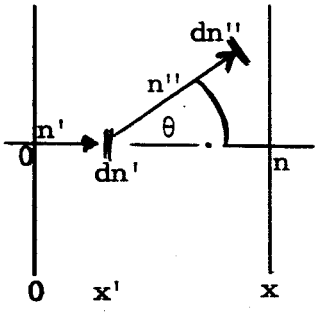

Probability that the neutron travels a distance x':

$$e^{-Nx'\sigma} = e^{-n'\sigma}$$ where σ = total cross section.

Probability that it is scattered in a layer dn':

$$dn'\sigma_n$$ where σ_n = scattering cross section.

Probability that the CMS scattering angle is θ_0:

$$d(\cos\theta_0)/2 = d\mu_0/2$$ (isotropic scattering).

Probability that the lab scattering angle is θ:

$$(d\mu/2)(d\mu_0/d\mu) \quad (\mu = \cos\theta).$$

Probability that the neutron travels a distance x'':

$$e^{-Nx''\sigma'} = e^{-n''\sigma'}.$$

Probability that it is captured within dn'':

$$dn''\sigma_\gamma'$$ (σ' and σ_γ' are the cross sections after the first collision).

The total probabilities for the combined events and for all possible combinations of n', θ, and n'' are

$$f_0 = \int_0^n e^{-n'\sigma}\, dn'\sigma_\gamma = (1-e^{-n\sigma})\frac{\sigma_\gamma}{\sigma} \quad . \tag{1}$$

$$f_1 = \int_0^n e^{-n'\sigma}\, dn'\sigma_n \left[\int_{-1}^0 \frac{d\mu}{2}\frac{d\mu_0}{d\mu}\int_0^{-n'/\mu} e^{-n''\sigma'}\, dn''\sigma_\gamma' + \int_0^1 \frac{d\mu}{2}\frac{d\mu_0}{d\mu}\int_0^{(n-n')/\mu} e^{-n''\sigma'}\, dn''\sigma_\gamma'\right] \quad . \tag{2}$$

For thermal neutrons the average energy loss in the scattering collision is zero, thus we can put $\sigma' = \sigma$ and $\sigma_\gamma' = \sigma_\gamma$. Since smooth cross sections are not affected by Doppler broadening we can also use the stationary target approximation. The latter yields

$$\frac{d\mu_0}{d\mu} = \frac{\left(\mu + \sqrt{A^2 - 1 + \mu^2}\right)^2}{A\sqrt{A^2 - 1 + \mu^2}} \tag{3}$$

For $A = \infty$, $\frac{d\mu_0}{d\mu} = 1$

In this special case we can carry out the integrations in (2). Define $F_1(\infty, s)$ by

$$f_1 \equiv \frac{\sigma_n \sigma_\gamma}{\sigma^2} F_1(\infty, s)$$

where $s = N\sigma$. Then the integrations yield:

$$F_1(\infty, s) = \tfrac{1}{2}\left[(1-e^{-s})^2 - (1-e^{-s})s\,Ei(-s) + (1+e^{-s})\left(Ei(-s) - \ln Cs\right) - Ei(-2s) + \ln 2Cs\right]$$

$$\approx \frac{s^2}{2}\left[-\ln Cs\left(1 - \frac{s}{2}\ldots\right) + \frac{3}{2} - \frac{5}{15}s\ldots\right]$$

where

$$Ei(-s) = \int_{-\infty}^{s} \frac{e^x}{x}\,dx = \ln Cs - \frac{s}{1\cdot 1!} + \frac{s^2}{2\cdot 2!} - \ldots.$$

$$\ln Cs = \ln C + \ln s = 0.57722\ldots + \ln s$$

$$f_0 = (1-e^{-s})\frac{\sigma_\gamma}{\sigma}$$

The geometric series approximation:

$$f = f_0 + f_1 + f_2 + \ldots. \approx f_0\left[1 + \frac{f_1}{f_0} + \left(\frac{f_1}{f_0}\right)^2 + \ldots\right]$$

yields

$$f \approx \frac{f_0}{1-\frac{f_1}{f_0}}$$

or

$$\frac{f_0}{f} = 1 - \frac{f_1}{f_0} = 1 - \frac{\sigma_n s^2}{2\sigma(1-e^{-s})}\left[-(.57722.. + \ln s)\left(1 - \frac{s}{2}\right) + \frac{3}{2} - \frac{5}{12}s\ldots\right]$$